Ocean Engineering 279 (2023) 114484

Contents lists available at ScienceDirect

Ocean Engineering

journal homepage: www.elsevier.com/locate/oceaneng

SPH modeling of dam-break bores on smooth and macro-roughness slopes

Chun-Cheng Chang, Yun-Ta Wu *

Department of Hydraulic and Ocean Engineering, National Cheng Kung University, Tainan City, 701, Taiwan

ARTICLE INFO

Handling Editor: Prof. A.I. Incecik

Keywords:
Dam-break
Bore
Swash flow
Runup
Macro-roughness slope
SPH

ABSTRACT

Understanding the kinematics and hydrodynamics of long waves in nearshore zones is currently one of the more pressing aims motivating research in the coastal engineering community. Owing to the simplicity of its setup, the dam-break mechanism is frequently adopted in laboratories to generate bores and model long-wave dynamics, kinematics, and runup processes in coastal regions. Numerical simulations have been used to replicate the results of laboratory experiments using a dam-break system. In this study, we aimed to evaluate the effect of different macro-roughness slopes owing to dam-break driven swash using an open-source particle-based program, DualSPHysics, based on smoothed particle hydrodynamics. To serve as a reference case, the swash flows of a dambreak-generated bore on a uniform slope were performed, and model–data comparisons were made for time-series analysis of the surface elevation, runup process and velocity profiles at selected points. Simulations of dam-break bores passing over slopes containing various configurations of macro-roughness elements were performed to replicate long waves impacting an array of structures in a waterfront area. Different configurations of slope roughness have varying effects on the flow hydrodynamics in the swash zone, which were examined in this study.

1. Introduction

Long waves such as tsunamis are natural hazards that affect regions worldwide. Wave runup can dislodge objects and convey them from coastal areas to areas farther inland, and the rundown process can wash cars, pieces of wood, and humans out into the ocean. Hence, it is vital to study the behavior of tsunamis and the risks they carry. Increasing our knowledge of the hydrodynamic processes in the swash zone is key to understanding the possible damage caused by tsunamis. Tsunamis have a variety of characteristics such as the velocity at which they move, the wave runup they cause, and the inundation left in the aftermath, which potentially influence their destructiveness. Therefore, several studies have been conducted to examine the behavior of tsunamis under various situations.

Tsunamis have been observed as undulating or breaking bores in the nearshore (e.g., Takahashi and Tomita, 2013). Several studies have simulated the hydrodynamics of tsunamis. Conidial waves and, in particular, solitary waves have frequently been used in simulation of tsunamis propagating in nearshore zones (e.g., Briggs et al., 1995; Li and Raichlen, 2003; Liu et al., 1995; Wu, 2022; Wu et al., 2018; Yeh et al., 1994). However, the properties of the solitary waves and bores differ significantly. Madsen et al. (2008) noted that a tsunami first breaks and then transforms into a bore during its propagation in the nearshore zone. Nevertheless, sufficient time and space are required for a bore transforming into a solitary wave. Furthermore, according to the theory of solitary waves, the characteristic wavelength of a solitary wave decreases with every incremental increase in the wave nonlinearity. Owing to the shoaling effect, the behavior of a shoaling solitary wave is quite different from that of a natural tsunami with a very long wavelength. This may result in an underestimation of inundation duration if a solitary wave is used to model the tsunami. Based on in situ experiments, it has been proposed that the front waves of a tsunami correspond in shape to the long waves in the small-amplitude wave theory, independent of the location of the waves (e.g., Chan and Liu, 2012). Furthermore, the wave steepness of solitary waves has been proven to be smaller than that of realistic tsunamis (Schimmels et al., 2016). These findings indicate that solitary waves may not be suitable for assessing the tsunami hazards. However, it is difficult to conduct an experiment to generate a tsunami that develops, propagates, shoals, and breaks with the characteristics of a bore. Alternatively, the dam-break mechanism is beneficial for generating different types of bores. By suddenly releasing the water stored upstream, a tsunami-like bore is formed following the propagation of a large volume released water. Owing to the similarity of tsunami-like bores in nature and their simple experimental setups, dambreak-generated bores have become important for studying the hydrodynamics and characteristics of swash flows (e.g., Kikkert et al.,

* Corresponding author.
E-mail address: ytwu@mail.ncku.edu.tw (Y.-T. Wu).

https://doi.org/10.1016/j.oceaneng.2023.114484
Received 29 November 2022; Received in revised form 3 March 2023; Accepted 6 April 2023
Available online 19 April 2023

2012; Kikkert et al., 2013; O'Donoghue et al., 2016; O'Donoghue et al., 2010; Pintado-Patiño et al., 2021). In addition, there are several ways to simulate tsunami hydrodynamics. For example, Asai et al. (2016) simulated a tsunami from its generation and propagation to inland inundation. The evolution of a gravity wave into a bore-like wave was simulated. However, based on the dam-break mechanics, a tsunami-like bore was directly generated to investigate its propagation in the nearshore and subsequent inland inundation.

To perform experiments on bores, it is necessary to classify their characteristics under various conditions. The Froude number, F, is used to categorize bores according to their flow intensities. Based on the Froude number and on whether or not a bore breaks, Miller (1968) refined the definition of bores by categorizing them as either weak bores ($F < 1.25$) or fully developed bores ($F > 1.55$). Furthermore, Yeh et al. (1989) used the dam-break mechanism to generate bores and, with this setup, they found that the ratio of the upstream and downstream volume of water could be used as a second criterion in the characterization of bores. These two criteria have been proven to be useful in existing studies. The Froude similarity between realistic tsunamis and dambreak-generated bores was shown in Barranco and Liu (2021). Their work on dam-break bores showed that the characteristic wavelengths of a bore and of the receding bore after its upwash vary according to the length of the wave upstream, where the water volume is stored, and downstream, where the bore develops, respectively. In a work that added to the understanding of the distinct properties of a wave in the upstream and downstream portions of a wave flume apparatus, Lin et al. (2020) found that non-decaying bores can be generated by adjusting the length of the wave upstream and downstream, regardless of the scale of the flume. Furthermore, the characteristics of the bores, including the runup height, runup duration and depth of inundation, were described by using the empirical formulas of Barranco and Liu (2021). Huang and Wu (2021) conducted flume experiments, whose dam-break configuration in terms of water volume stored and distance for bore development was different from that of Barranco and Liu (2021). They showed that, for non-decaying bores, using the same water depth upstream and downstream of the gate, the main waveforms at different locations as well as the resulting runup heights matched the measured data of Barranco and Liu (2021), although the wavelengths of the bores were different between these two experiments owing to the variation in the wave volume stored upstream of the gate. Huang and Wu (2021) expanded the dam-break conditions that Barranco and Liu (2021) did not reach and further extended the runup and inundation formulations of Barranco and Liu (2021) by incorporating their new experimental data. Further, the classifications of bore types were revised based on experimental observation in Huang and Wu (2021) for weak bores ($F \leq 1.28$), transitional bores ($1.35 \leq F \leq 1.50$), and fully developed bores ($F \geq 1.50$).

State-of-the-art experimental studies using the dam-break mechanism to generate bores have made valuable contributions to the efforts to decipher the hydrodynamic processes underlying the behavior of long waves. The addition of macro-roughness elements such as buildings and vegetation to a dry bed is significant because it realistically models the structures found in actual coastal zones. The runup of long waves and wave-induced loading on coastal structures has been studied by several researchers. Simamora et al. (2007) developed physical models of coastal buildings, that were prioritized in evacuation plans during tsunami events and conducted tests by producing tsunami bores with a paddle mechanism. The forces exerted on the buildings were recorded and analyzed to estimate the loads that a building deemed safe would need to withstand. In another set of experiments, Chuang et al. (2020) used a large cube, an idealized model for nearshore buildings, instrumented with load cells, and exposed it to the impact of a tsunami-like bore produced by a piston-type wavemaker. Detailed measurements of the flow velocities of the bores and the pressures and forces induced by the bores were obtained when the cube was placed at different positions and angles in relation to the incoming bores. Goseberg (2013) used macro-roughness elements with building models designed on a 1/40 scale. The results showed that different arrangements of cubes and the spaces between them significantly affected the runup and reflected waves after the impact.

Although long-wave runup in conjunction with macro-roughness elements has been studied, some limitations remain in the existing experimental studies owing to the limited equipment used for measuring the flow characteristic of the entire wave flume. Furthermore, varying the geometric arrangement and structural configuration in a laboratory is time-consuming and expensive. It is easier to achieve a more complete perspective using numerical simulations. To this end, various numerical methods have been applied to study swash flows in bores. Zhang and Liu (2008) used two-dimensional (2D) Reynolds–averaged Navier–Stokes (RANS) equations with a rotated coordinate system that aligned the sloping beach for parallel and orthogonal beds to enhance the resolution of the swash flow characteristics for the partial-cell modeling framework. The rotated coordinate system was later used by Torres-Freyermuth et al. (2013) and Pintado-Patiño et al. (2015) for dam-break driven swash flows over rough impermeable and permeable slopes, respectively. To model the detailed wave breaking processes, complex topographies, and macro-roughness features, such as the numerical model of nearshore buildings in three dimensions (3D), should be applied (e.g., Kim et al., 2017). Qin et al. (2018) used a 3D RANS-based model to simulate tsunami overland flows around macro-roughness elements and the forces on these structures. Moris et al. (2021) experimentally identified the shield effect produced by building arrays impacted by tsunami-like waves generated by a wavemaker. They also performed numerical simulations based on 3D RANS modeling, particularly focusing on the load reduction caused by this shield effect.

In addition to mesh-based modeling, particle-based mesh-free numerical models such as the smoothed particle hydrodynamics (SPH) method, have been another reliable tool to model swash flows of bores. The SPH method was first introduced by Gingold and Monaghan (1977) and Lucy (1977) in astrophysics. After decades of development, it has become available for simulating the fluid dynamics of nearly incompressible fluids (e.g., Gomez-Gesteira et al., 2010; Monaghan, 1994; Monaghan et al., 2003). SPH-based models can be categorized into weakly compressible and incompressible methods. In the weakly compressible SPH (WCSPH) framework, the fluid pressure is explicitly linked to the fluid density using an equation of state to model the fluid as weakly compressible. In the incompressible SPH (ISPH) method, the fluid pressure is solved using a pressure Poisson equation (PPE) based on Chorin's projection scheme (Chorin, 1968). The semi-implicit scheme of the ISPH method considerably reduces spurious fluctuations, which is its primary advantage over the WCSPH method. However, the solution procedure of PPE in a projection-based scheme is time-consuming. Lo and Shao (2002) and Shao and Lo (2003) pioneered the use of ISPH to simulate free-surface flows. Continuous developments in WCSPH and ISPH are ongoing and the developed models have been widely used in hydraulics (e.g., Gu et al., 2022; Nóbrega et al., 2020) and coastal and ocean engineering (e.g., Chen et al., 2023; Khayyer et al., 2021). Luo et al. (2021) conducted a comprehensive review of the SPH-based methods for coastal and ocean engineering applications. Several studies have used WCSPH models to simulate the runup of solitary waves and periodic waves, and the results showed a high degree of agreement with empirical formulas and experimental data (e.g., Roselli et al., 2019; Shadloo et al., 2015). However, the dam-break problem has been largely used to validate the SPH-based model in terms of detailed free-surface evolution and its interaction with different types of structures (e.g., Ng et al., 2020; Wei et al., 2015) to facilitate the understanding of fluid–structure interactions. Existing studies have successfully simulated free-surface elevations and the associated forces on structures. Nevertheless, there is a conspicuous lack in the current research of studies using SPH models to perform detailed model–data comparisons for the velocity fields of a dam-break driven swash, indicating that the momentum of such violent free-surface flows cannot be determined. Several studies have identified that although a numerical model can accurately predict the free-surface elevations for a specific problem, modeling the associated flow fields remains challenging [see Chang et al. (2005)]. Accurate prediction of flow velocity is one of the key issues related to loading on structures and even sediment transport. Model–data comparison for the flow fields in the swash zone can further clarify the advantages and disadvantages of the SPH code used herein, which has not yet been performed.

This study aimed at numerically simulating dam-break driven swash due to bore uprush on smooth slopes, serving as a reference case, and macro-roughness slopes, representing an idealized and scaled coastal community, by using the open-source SPH code, DualSPHysics (Domínguez et al., 2022). Detailed model–data comparisons were performed for free-surface elevation, velocity and runup height for smooth and rough slope cases against the measured data of Huang and Wu (2021). Furthermore, the effects on the runup of varying the configurations of the macro-roughness elements were evaluated, which was the focus of this study.

2. Numerical model

2.1. Model description

DualSPHysics (Domínguez et al., 2022) is a modeling tool that allows user to solve continuity and momentum equations based on the Lagrangian meshless method. In fluid dynamics, DualSPHysics is used to solve discretized Navier–Stokes equations and to analyze the physical properties of fluids. In this model, the fluid is represented by several discretized particles, each of which has individual properties, such as mass, density, velocity, acceleration, and pressure. The technique of smoothing the kernel function is used to determine the properties of each particle. This involves integrating the properties of several particles in a kernel and thereby approximating the properties of a specific particle with kernel functions (Monaghan, 2005; Violeau, 2012). Thus, DualSPHysics can be used to study problems for which Eulerian methods may be difficult to apply, such as multi-phase flows and complicated geometries. In this study, DualSPHysics was employed to model swash flow hydrodynamics. In the following sections, we present an overview of DualSPHyics.

2.2. Functions in DualSPHysics

2.2.1. Governing equations

The continuity equation (CE) and momentum equations (MEs) are used in DualSPHysics as the governing equations for the model. Solutions of the CE and MEs are obtained based on the assumption of a WCSPH method. The pressure and velocity terms in the CE and MEs as well as the dissipation term in the MEs are incorporated into the SPH formulation using the smoothing kernel and discretization [see Violeau and Issa (2007)]. The original forms of the CE and MEs used in DualSPHysics are represented by Equations (2-1) and (2-2).

$$\frac{d\rho}{dt}+\rho\nabla\bullet v=0 \tag{2-1}$$

$$\frac{dv}{dt}=-\frac{1}{\rho}\nabla P+g+\Gamma \tag{2-2}$$

where ρ stands for the fluid density, t is time, P is the pressure, v is the velocity vector, g is the gravitational acceleration, and Γ denotes the dissipation term in the original momentum equation.

Two steps are generally adopted to apply the governing equations in the SPH method, kernel and particle approximations. First, a given function F can be represented in integral form.

$$F(r)=\int_{\Omega}F(r')W(r-r',h)dr' \tag{2-3}$$

where Ω is the computational domain, F is any variable, r is the position vector of F, r' stands for the integral approximation and h corresponds to the smoothing length, which determines the supporting area of the smoothing function. Any variable F at position r can be written as the product of a kernel function W.

In the second step, considering particle a, Equations (2-3) is approximated by summing the contributions from all neighboring particles,

$$F(r_a)\approx\sum_b F(r_b)W(r_a-r_b,h)\frac{m_b}{\rho_b} \tag{2-4}$$

in which r_b stands for the position vector of particle b, m indicates the mass of the specific particle, and ρ stands for the density of the specific particle.

By applying discretization to the governing equations, the CE and MEs can be represented as:

$$\frac{d\rho_a}{dt}=\rho_a\sum_b\frac{m_b}{\rho_b}v_{ab}\bullet\nabla_a W_{ab}+D_a \tag{2-5}$$

$$\frac{dv_a}{dt}=-\sum_b m_b\left(\frac{P_b}{\rho_b^2}+\frac{P_a}{\rho_a^2}+\Pi_{ab}\right)\bullet\nabla_a W_{ab}+g \tag{2-6}$$

where W_{ab} is the abbreviation of kernel function $W(r_a-r_b,h)$ [the Wendland function is used in this study (Wendland, 1995)]; D_a represents the density diffusion term [see Antuono et al. (2012) and Fourtakas et al. (2020) for detailed formulations]; v_{ab} represents the difference in velocity between particles a and b, i.e., v_a-v_b; and Π_{ab} is the viscosity term (see Section 2.2.2).

The solutions of the converted governing equations allow all the processes involved in the numerical differentiation of the equations to be performed without any grids. This helps the models operate in the Lagrangian simulation. However, to express the equations plainly, several extended terms or states in the SPH-based governing equations must still be determined or satisfied. The detailed mathematical formulations, numerical algorithms, and implementations are available in Crespo et al. (2015) and Domínguez et al. (2022). The following sections introduce the functionalities employed in the study.

2.2.2. Viscosity treatment

In the models created using DualSPHysics, two schemes are introduced for fluid simulations: (1) artificial viscosity and (2) laminar viscosity and a sub-particle-scale (SPS) turbulence model. In the SPS model, the turbulence is determined by the Smagorinsky subgrid model, which essentially originates from the large eddy simulation (LES). It is difficult to ensure that the correct turbulent characteristics can be resolved for the lack of high resolution when using the LES (e.g., Wu et al., 2014). Consequently, in this study, an artificial viscosity method, that has been widely used in the literature (e.g., Ng et al., 2020; Roselli et al., 2019), is adopted.

Artificial viscosity was introduced to determine the viscosity of a fluid in the SPH model (Monaghan, 1992), and this scheme is widely used in DualSPHysics. The viscosity term Π_{ab} can be expressed as

$$\Pi_{ab}=\begin{cases}\dfrac{-\alpha\overline{c_{ab}}\mu_{ab}}{\overline{\rho_{ab}}}, v_{ab}\bullet r_{ab}<0\\ 0, v_{ab}\bullet r_{ab}>0\end{cases} \tag{2-7}$$

where v_{ab} and r_{ab} are the difference in velocity and position, respectively, between particles a and b; $\mu_{ab}=h_s v_{ab}\bullet r_{ab}/(r_{ab}^2+\eta^2)$, with h_s denoting the smoothing length, $\eta^2=0.01{h_s}^2$, and $\overline{c_{ab}}=0.5(c_a+c_b)$ representing the mean speed of sound. The coefficient α is determined

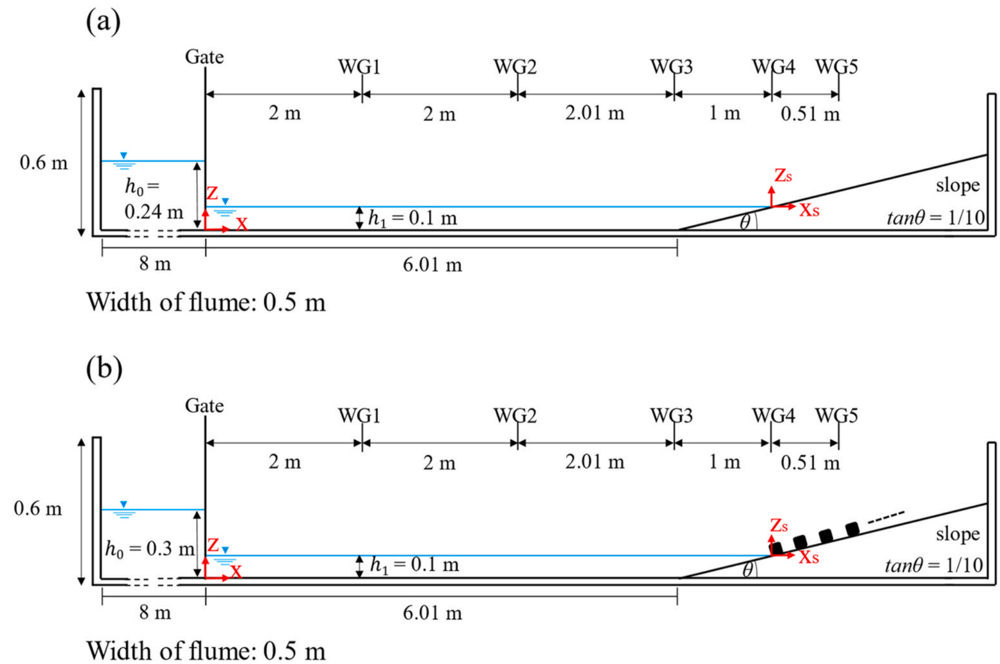

Fig. 1. Diagrams of the experimental setup in Huang and Wu (2021). Simulations in this study follow this setup, where (a) shows a smooth slope and (b) represents a slope with macro-roughness elements (not to scale).

depending on the model, and controlling it allows the identification of the correct dissipation rate for each model. Altomare et al. (2015) suggested assigning a value of $\alpha = 0.01$ in ordinary studies of the effects of wave propagation and wave loading on coastal structures. Throughout this study, the estimation of artificial viscosity in the simulations is made based on the previous studies for using $\alpha = 0.01$.

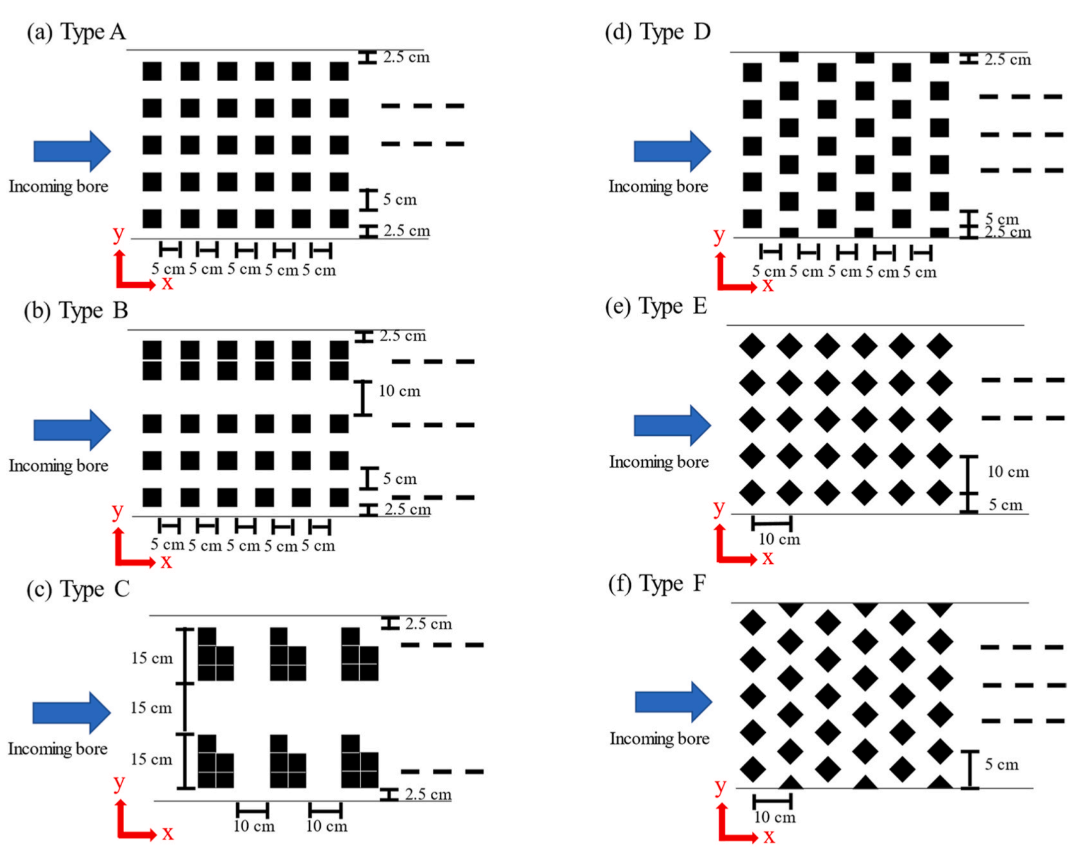

Fig. 2. Diagrams of six different configurations of macro-roughness elements, where (a) the original replicates the experimental setup and (b–f) represent additional macro-roughness cases for the numerical simulations.

2.2.3. Equation of state

To fulfill the assumption of weak compressibility in the DualSPHysics application [see Monaghan (1994)], decreasing the speed of sound is necessary to remain the time steps imposed by the Courant condition. The relationship between the fluid pressure and particle density can be expressed as:

$$P = \frac{c_0^2 \rho_0}{\gamma}\left[\left(\frac{\rho}{\rho_0}\right)^{\gamma} - 1\right] \tag{2-8}$$

where $\gamma = 7$, $\rho_0 = 1000\ kg/m^3$, and $c_0 = c(\rho_0) = \sqrt{\frac{\partial P}{\partial \rho}\Big|_{\rho 0}}$ representing the speed of sound at the reference density. The ratio of $c_0/\ u_{max} \geq 10$ is practicable that can remain the governing equations explicitly decipherable, allowing only approximately 1% of the variations in the density of fluid followed.

2.2.4. Boundary condition and time-stepping method

Modeling the boundary layer in a flow is challenging in the SPH framework. A dynamic boundary condition (DBC) was used in this study (Crespo et al., 2007). In this approach, the boundary particles satisfy the same CE as fluid particles. Therefore, the advantage of the DBC is its computational simplicity, because the boundary and fluid particles can be calculated inside the same loops, thus the DBC can be straightforwardly used to represent flows over complex shaped geometries. This feature was particularly important in this study when complicated macro-roughness elements were simulated. To approximate the no-slip boundary condition in the DBC, the velocities of the boundary particles were set to zero at the solid boundaries. As the density of the boundary particles increases locally, the pressure term increases in the momentum equation; thus, the force exerted on the fluid particle also increases, which defines the repulsive force between the boundary and fluid particles. Consequently, this boundary maintains a certain distance between the boundary and the fluid particles, which was found to be less than twice the smoothing length h (Roselli et al., 2019). More detailed information is available in Crespo et al. (2007).

In terms of the time-stepping method, the Verlet scheme (Verlet, 1967), which features a low computational cost, was applied in this study (Domínguez et al., 2022). Moreover, the time integration is bounded by the Courant–Friedrich–Levy (CFL) condition, which should be satisfied in explicit time-integration schemes. In this study, the Courant number (CFL) was set at 0.2.

3. Physical experiment and numerical setup

Huang and Wu (2021) conducted experiments on dambreak-generated bores on smooth and macro-roughness slopes at the Department of Hydraulic and Ocean Engineering, National Cheng Kung University, Taiwan. In this study, we first performed numerical simulations using DualSPHysics to replicate the aforementioned experiments for dam-break driven swash flows. In the following, we briefly report the experimental configurations and the corresponding setup in numerical modeling.

3.1. Laboratory experiment

Experiments by Huang and Wu (2021) were conducted using a sectional wave flume with a length of 25 m, 0.5 m in width and 0.6 m in height. A gate located at one end of the flume, which was moved vertically using a servo-controlled motor, separated the flume into two sections: an 8 m long storage section (where the water is stored) and a 6.01 m long developing section (where the bore develops). A sketch of the flume and definitions of the variables used are shown in Fig. 1. A 1/10 sloping beach was installed at the other end of the flume, where the slope was either smooth or contained macro-roughness elements in different configurations. The slope was entirely made of plexiglass for the smooth case [see Fig. 1 (a)] whereas for the macro-roughness slope, the plexiglass slope was covered with an array of cubes, each of which had the same dimensions (5 cm × 5 cm × 5 cm) [see Fig. 1 (b) and Fig. 2 (a)]. The cubes located near the flume walls were fixed at a distance of 2.5 cm from the sidewalls, with a distance of 5 cm separating all cubes in the arrangement. There were 25 rows of 5 cubes each, for a total of 125 cubes.

Five ultrasonic sensors were placed at 2, 4, 6.01, 7.01 and 7.51 m from the origin at the dam-break gate, to measure the free-surface elevations. The sensors were installed at the center line of the flume in the lateral direction, which is 0.25 m from the sidewalls. These measuring sensors were synchronized with the dam-break gate for a 100 s recording with a 100 Hz sampling rate. The maximum runup heights were measured using a high-definition webcam (BRIO 4K, Logitech) with a frame rate of 60 frames per second (fps) and digital image processing (e.g., Wu et al., 2021; Wu et al., 2022). The velocity fields near the shorelines were measured using particle image velocimetry (PIV), consisting of a 5 W continuous laser and a high-speed camera (Phantom VEO-E 340L) with a resolution of 2,560 × 1,000 pixels at a sampling rate of 1,000 fps. These preliminary velocity characteristics obtained from an instantaneous experimental realization were briefly reported in Hsiao and Wu (2022) for the smooth case but not for the macro-roughness case.

3.2. Numerical model setup

In this study, the computational domain was the same as that of the experimental flume and discretized into a collection of particles in DualSPHysics. The effect of the particle size was investigated and judged by means of model–data comparisons. A detailed comparison of using different particle sizes is presented in Appendix A.1. It was found that using a particle size of less than 0.005 m the numerical results in terms of free-surface fluctuation and runup height could not be improved significantly when compared with the experimental data. For the smooth slope case, the numerical model was setup in 2D, and the particle size was reduced to 0.001 m to achieve a better resolution when compared with the PIV measurement. For the macro-roughness slope case, it was necessary to build the model in 3D because of the complexity of the macro-roughness features and the interaction between the bore and each element. A particle size of 0.005 m was therefore utilized for 3D cases.

Comparisons of the free-surface elevation and inundation distance in the time series between the 2D and 3D simulations for the smooth slope case can be found in Appendix A.2. For both the 2D and 3D numerical simulations, the dam-break gate was modeled as an instantaneous gate removal. Moreover, different ratios between the water-depths upstream and downstream of the gate were used, i.e., $h_1/h_0 = 24/10$ and 30/10 for the smooth and macro-roughness slopes, respectively. Both cases were fully developed, and the wavefront breaks as soon as the gate was opened and satisfied the non-decaying bore definition of Barranco and Liu (2021).

The smooth slope was simply implemented as a smooth material in DualSPHysics, whereas the macro-roughness slope was arranged in the same manner as in the experiment, and the slope and element surfaces are also implemented as smooth. These numerical roughness elements were modeled as bathymetry, which was generated using an open-source 3D illustrator, called Blender. The numerical macro-roughness slopes can be easily established by providing the geometries of the slopes as STL files. Fig. 2 (a) shows the original configuration used to replicate the experimental setup.

Generally, the arrangements and design of streets and buildings in waterfront areas depend on their locations. Onshore structures arranged in a combination of staggered and non-staggered patterns can be observed in a single coastal community (e.g., Qin et al., 2018; Prasetyo et al., 2019). The macro-roughness arrangement used in this study was essentially based on the common layout of coastal buildings and

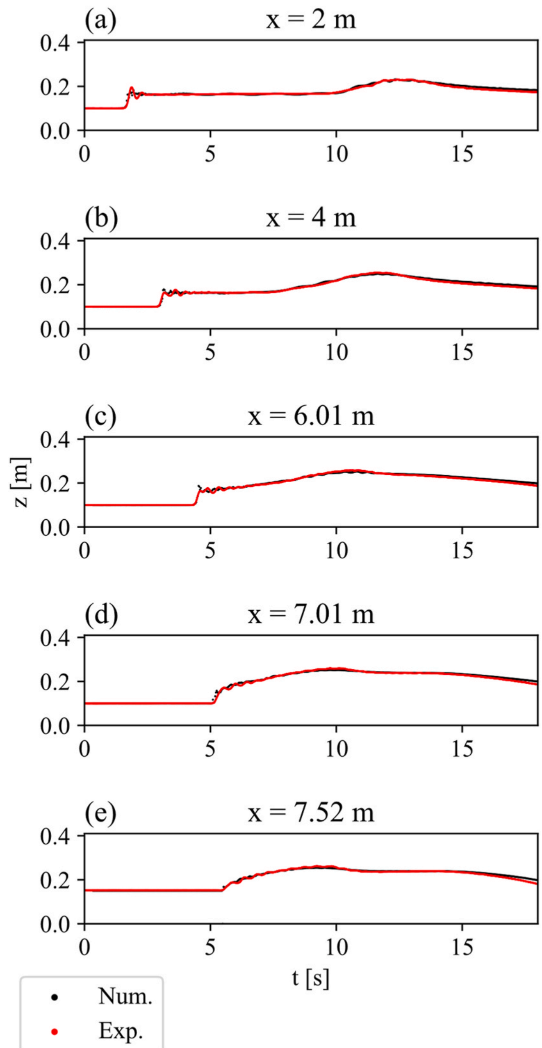

Fig. 3. Model–data comparison of free-surface elevation in time series at different locations for dam-break driven swash on the smooth slope, where $h_1/h_0 = 24/10$ and $h_0 = 10$ cm.

relevant studies, in which rectangular buildings and structures are possible. Five additional numerical simulations in 3D were conducted by varying the arrangement of the roughness elements (see Fig. 2). The Type A configuration aims to simulate a simplified geometry, identical to that used in Huang and Wu (2021) and similar to those of Moris et al. (2021) and Zhang et al. (2023), The Type B scenario targets the change in the width of the main street, and the Type C case scenario mimics a complex building layout in a real community (Qin et al., 2018). Similar to that used by Goseberg (2013), Type D is a staggered version of Type A, Type E is a non-staggered and rotated configuration, and Type F is a staggered and rotated configuration. We note here that the size of each element, the number of elements used, and the ratio of the projected area of the elements onto the slope for these six configurations were identical. Thus, the extent of runup and inundation can be compared on the same basis, with the aim of providing useful information for the urban design of nearshore buildings and streets.

4. Results and discussion

4.1. Dam-break driven swash on a smooth slope

In this section, we present the results obtained from model–data comparisons in terms of free-surface elevation, velocity fields and inundation distance for swash flows generated by dam-break bores on a smooth slope.

4.1.1. Free-surface elevation

The measured data obtained from five wave gauges, whose corresponding instrumented locations are shown in Fig. 1, were compared with the numerically simulated results using DualSPHysics. Fig. 3 shows the model–data comparison of the time series of the free-surface elevation at different locations, where the black dots represent the results of the numerical simulation and the red dots represent the mean values of the experimental data. The duration of the numerical simulation was 24 s, with t = 0 s representing the moment when the gate was opened in the experiments.

We note here that, in the numerical simulation, the dam-break gate is modeled as an instantaneous gate removal, which is different from that of the physical experiment. In Wu and Huang (2020), the same smooth-slope experiment was used for comparison with the simulated results using a well-validated model based on the RANS equations along with a non-linear turbulence closure model (Lin and Liu, 1998). A comparison between measured and RANS-simulated results indicated that the lifting speed of the dam-break gate can be considered instantaneous for free-surface elevations and runup heights. The lifting speed of the gate opening resulted in a slight phase variation in the leading wavefront. In this study, the numerical results were consistently shifted 0.3 s to fit the data. In addition to the phase variation, the agreement between the measured and modeled results was generally good.

In terms of bore characteristics, Fig. 3 (a) shows the turbulent bore front ($t < 2$ s) connected to a bore plateau ($2 \text{ s} < t < 10$ s), which is

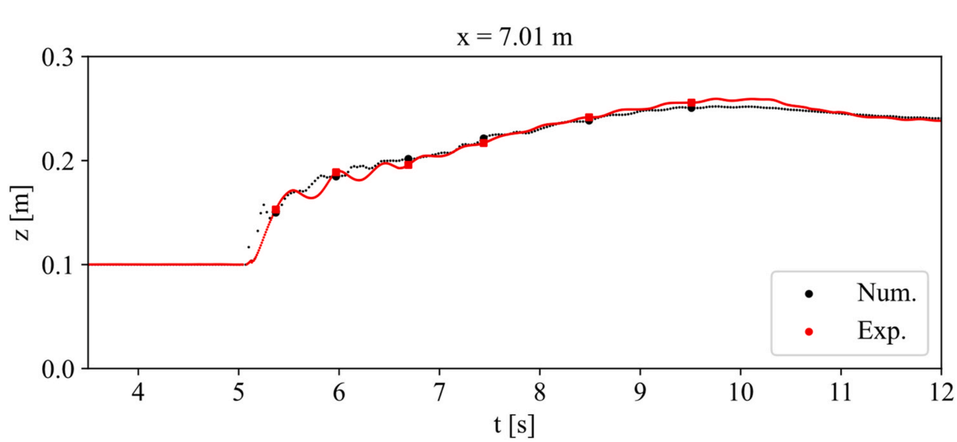

Fig. 4. Model–data comparison of the free-surface elevation in time series at the shoreline. The points in this diagram correspond to the different time instants in Fig. 5 for dam-break driven swash on the smooth slope, where $h_1/h_0 = 24/10$ and $h_0 = 10$ cm.

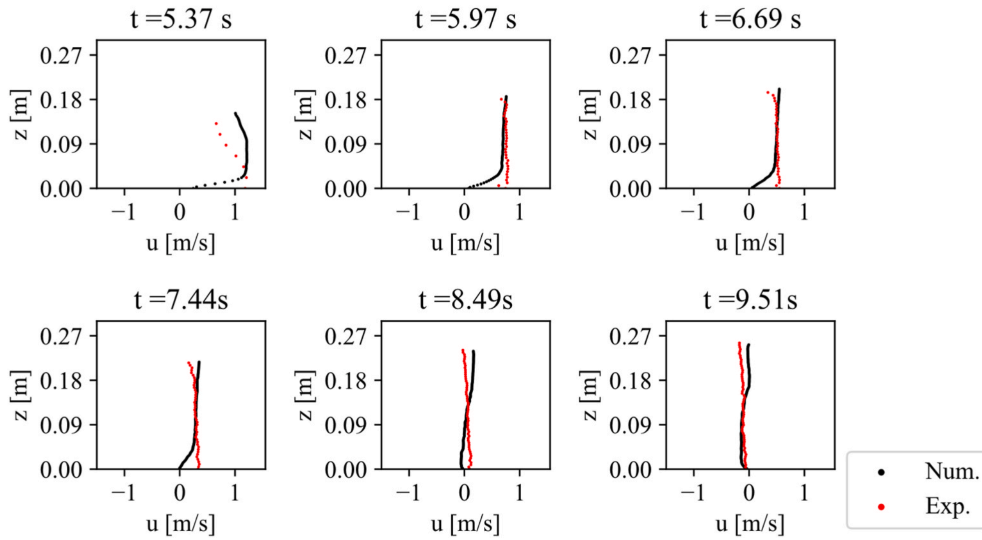

Fig. 5. Model–data comparison of velocity profiles at the still-water shoreline for selected time instants. This case is for dam-break driven swash on the smooth slope, where $h_1/h_0 = 24/10$ and $h_0 = 10$ cm.

attributed to the sufficient length of the dam-break reservoir for generating a fully developed and non-decaying bore. For t > 10 s, the fluctuation is due to wave reflection from the sloping beach. Fig. 3 (d), whose measurement location is at the still-water shoreline, shows the inundation depth, which is defined as the maximum surface elevation recorded at this point, and the flooding plateau. Model–data comparison shows that the variation in the inundation depth is around 2.6%, in which the variation between the measured and modeled results is similar to that of Barranco and Liu (2021), who used a non-hydrostatic wave-flow model to simulate a dam-break driven swash on a planar slope.

4.1.2. Velocity field

In this sub-section, a model–data comparison was made for the velocity profiles at the still-water shoreline. Fig. 4 shows the details of the bore front time series, which is identical to that shown in Fig. 3 (d), but with a shorter time axis. As shown in Fig. 5, six representative time instants were selected to demonstrate the horizontal velocity profiles (u) at locations corresponding to those shown in Fig. 4. The maximum flow velocity was observed at t = 5.37 s for the bore approaching the still water shoreline. Afterward, the flow velocity decreases from $u \approx 0.8$ m/s to 0.2 m/s corresponding to t = 5.97 s to 7.44 s, respectively. Then, the flow reaches a nearly quiescent state, i.e., $u \approx 0$, although the free-surface elevation is still increasing. After the free-surface reaches its highest elevation, i.e., the maximum inundation depth, the flow starts to retreat into the offshore direction, i.e., $u < 0$, which can be observed at t = 9.51 s. We note here that the detailed swash flow fields have not been reported in Hsiao and Wu (2022). Herein, only the overall flow characteristics are presented, with a focus on the accuracy of the numerical model.

The model–data comparison shows that the free-stream velocity profiles at different time instants between the measured and modeled results are mostly similar, except for that at t = 5.37 s, and the maximum discrepancy between the two results is approximately 12%. At this instant, a shock wave featuring a turbulent bore front consisting of entrained air bubbles approaches the swash zone, causing large variations in the water surface profiles (see Fig. 4). Some splashing features of broken waves, i.e., discontinuous free-surface fluctuations, can be observed in the numerical results. Such violent free-surface flows remain challenging and uncertain in both the experimental and numerical modeling. A similar phenomenon, in which the measured and modeled results were not highly correlated on the turbulent wavefront, was also noted by Wang and Liu (2022), who developed an ISPH model for simulating breaking periodic waves in the surf zone.

In terms of the velocity profiles beneath the free-stream velocity, as mentioned in Section 2.2.4, the boundary layer in the flow is a challenge in SPH modeling. Model–data comparison obviously shows large differences near the bottom boundary during wave uprush, i.e., t = 5.37 to 7.44 s. The inconsistency of the boundary layer between the physical and numerical modeling results was also reported by Roselli et al. (2019) and Wang and Liu (2022) for simulating surf flows generated by periodic breaking waves using SPH-based models. This variation was mainly due to the particle size used and the implementation of the DBC at the bottom boundary in this study. As reported by Roselli et al. (2019), who used DualSPHysics to simulate periodic wave breaking in the surf zone, the use of the DBC explains the differences in velocities near the seabed owing to the presence of a repulsive force between the boundary and fluid particles, which may lead to unphysically large boundary layers in

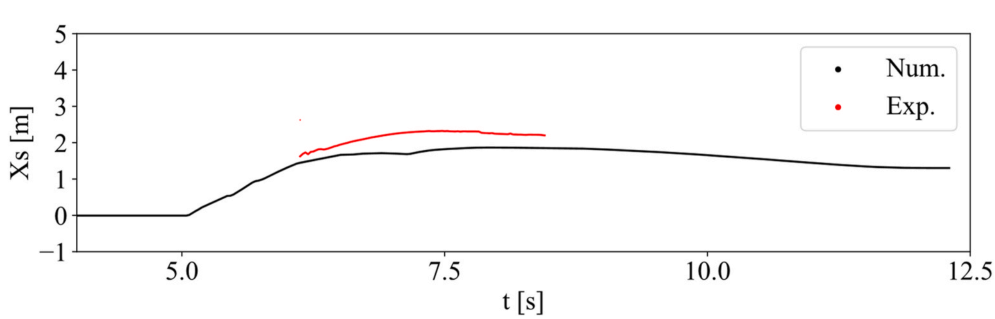

Fig. 6. Model–data comparison of inundation distance in time series for dam-break driven swash on the smooth slope, where $h_1/h_0 = 24/10$ and $h_0 = 10$ cm.

the flow (English et al., 2022). Recently, English et al. (2022) proposed the modified dynamic boundary condition (mDBC) in DualSPHysics to palliate the boundary layer "gap" issue in DBC, which deserves further investigations to compare the simulated results using these two boundary conditions.

One of the challenges in modeling swash flows is the flow transition from a wet zone to an initially dry area. Higuera et al. (2018) studied the swash flows generated by a solitary wave on a steep slope and found phase differences during wave runup between the results obtained from 3D RANS modeling and PIV measurements. The phase inconsistency of the wave runup until the shoaling wave reaches the maximum runup height leads to further variation compared to the flow fields during the wave rundown. To obtain a fair judgement for model–data comparison, Higuera et al. (2018) used the time when the maximum shoreline excursion occurred as the starting phase for comparison with the downrush flow characteristics. In this study, the time at which the runup phase ends in both the measurements and simulations is almost the same, i.e., t = 7.44 s, although the maximum runup heights are considerably different, which will be discussed in the next section. Therefore, using this method to reset the time for rundown flows cannot improve the fit of these two results based on the numerical results presented herein.

4.1.3. Inundation distance

Fig. 6 shows the model–data comparison of the inundation distance in the time series, with the x-axis representing the maximum inundation distance along the horizontal axis (i.e., X_s, see Fig. 1 for definition), where the maximum excursions in this plot can be considered as the maximum runup heights. Clearly, the simulated maximum inundation distance is smaller than that in the experiment, i.e., 2.32 m and 1.87 m for the measured and modeled results, respectively. A relative error of approximately 19% is observed in the numerical simulation. Such an underestimation of the inundation distance is sometimes mentioned in studies using SPH-based models although the use of these models to simulate swash flows and moving shorelines is relatively limited. Roselli et al. (2019) employed DualSPHysics to model surf flows generated by periodic waves, and the maximum runup heights of different types of breaking periodic waves were discussed based on their simulated results. They found that the simulated runup heights were consistently smaller than those predicted by the empirical runup formulas. Shadloo et al. (2015) used the GPUSPH model to simulate the runup of solitary waves. They obtained satisfactory agreement from model–data comparisons for the free-surface elevation time series. However, they found the underestimation of maximum runup heights when comparing with the experimental data. They claimed that this discrepancy was associated with the use of an artificial viscosity. The small runup can also be explained by comparing the measured flow velocities in Section 4.1.2. In particular, the thick boundary layer found in the numerical simulation suggests a high viscosity effect, and thus a small runup height.

In short, some discrepancies during wave uprush can be found in the model–data comparison, as a result of the energy dissipation that occurs at the boundary between the wet and dry surfaces. It should also be noted that the runup of the dambreak-generated bore is different from that of both periodic and solitary waves. This is because the breaking of a fully developed bore occurs before it reaches the slope, which makes the water flow characteristics more complicated and disorderly. Therefore, inaccuracies may be accumulated in numerical simulations and thereby influence the runup of dam-break bore on a sloping beach. However, with the exception of these slight problems, the hydrodynamic analysis of the bore performed using DualSPHysics exhibited a good fit with the experimental data.

4.2. Dam-break driven swash on a slope covered with macro-roughness elements

In this section, model–data comparisons are presented in terms of free-surface elevation, flow patterns, and inundation distance for swash flows generated by dam-break bores on a macro-roughness slope. The numerical simulation for Type A, as shown in Figs. 1 (b) and 2 (a), were performed in 3D to include the complicated geometry of the rough slope. Additional 3D simulations were performed to adjust the element configurations of the macro-roughness slopes, which are discussed in the following section.

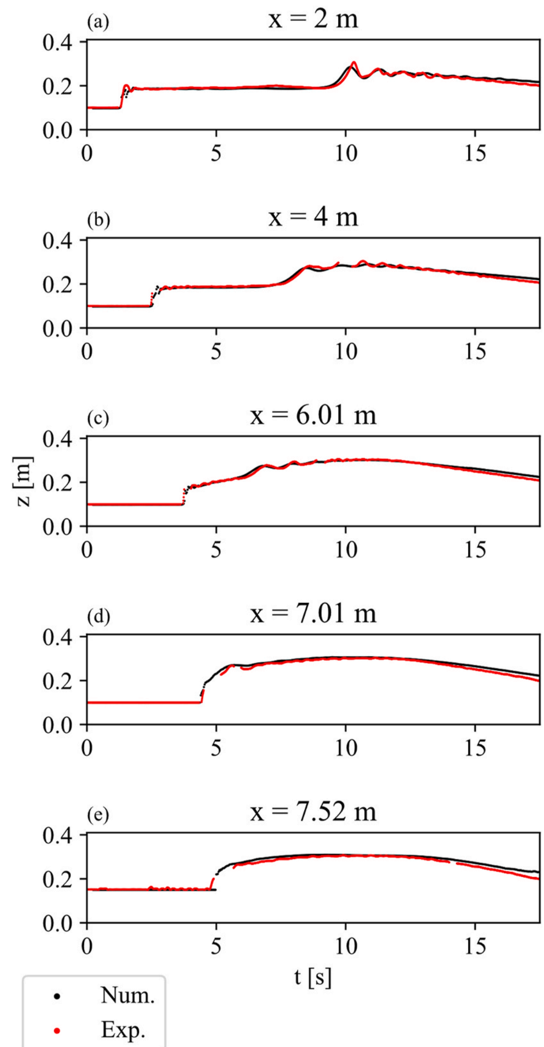

Fig. 7. Model–data comparison of free-surface elevation in time series for the Type A configuration of macro-roughness slope, where $h_1/h_0 = 30/10$ and $h_0 =$ 10 cm.

4.2.1. Free-surface elevation

As mentioned in Section 3.1, for the macro-roughness slope case of the Type A configuration (see Fig. 2), the water depth ratios are $h_1/h_0 =$ 30/10 and $h_0 = 10$ cm, such that the generated bore in terms of the wave height is slightly higher than that of the smooth case. Fig. 7 shows model–data comparison of the time history of the free-surface elevation at different locations. Similarly, the dam-break gate is modeled as an instantaneous gate removal, which is different from that of the experiment. Thus, the numerical results are consistently shifted 0.2 s to fit the leading bore front recorded at WG1 in 3D simulations.

Before the dam-break bore uprushes the slope, the overall free-surface evolution process is similar to that of the smooth case. Fig. 7 (a) shows a turbulent bore front propagating in a constant–depth region with a long-bore plateau (1 s < t < 9 s). Unlike the smooth case, which exhibits only one significant reflection from the slope [see Fig. 3 (a)],

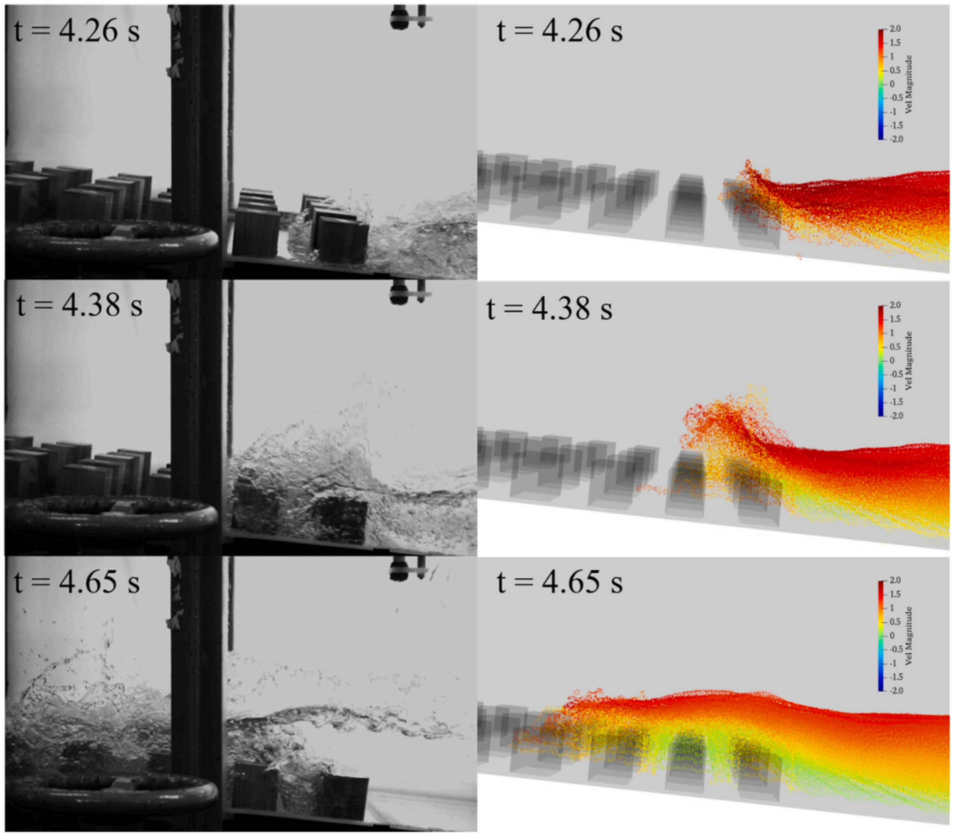

Fig. 8. Comparison of flow patterns at different time instants between laboratory observation (left panels) and SPH modeling (right panels), where $h_1/h_0 = 30/10$ and $h_0 = 10$ cm. The colorbar in the numerical simulations indicates the velocities of particles in the x-direction (unit: m/s).

undulating reflection tails can be observed in Fig. 7 (a), approximately in between 9 s < t < 14 s, owing to the complexity of the macro-roughness features. At the still-water shoreline [Fig. 7(d)], a flooding plateau between 6 s < t < 14 s was observed without a significant surface elevation peak to identify the inundation depth, which was different from that of the smooth case. A possible reason for this is that the presence of macro-roughness blocks the uprush flows, thereby reducing the flow velocity. It is speculated that the water mass is accumulated in the swash zone supported by the long-bore plateau, which causes the water surface to remain nearly constant during the inundation stage.

Some missing data points were found near the bore front in the experiment, as shown in Fig. 7(d and e). This is because the ultrasonic sensors used in the experiment to record free-surface elevations may not work well in measuring bubbly flows (e.g., Wu et al., 2021), especially during the bore interactions with the slope covered with macro-roughness elements. To avoid confusion, the nosing data has been removed from the model–data comparison presented in Fig. 7. Overall, the model–data comparison shows satisfactory agreement between the measured and model results. Slightly phase variation can be found for wave reflection from the slope [see Fig. 7 (a) at t ≈ 10 s]. The reason for this discrepancy is the complicated downrush flows that cannot be properly simulated in the numerical model. Further analysis of the flows during the rundown stages is presented in the following sections.

4.2.2. Flow pattern

Because PIV measurements are not available for the rough slope case, in this section, we present a qualitative examination of the behavior of a bore crashing on a slope covered with a layer of macro-roughness elements. The model–data comparisons are shown in Fig. 8. The snapshots of the flow pattern in the laboratory experiments are shown for the following times: t = 4.26 s, t = 4.38 s, and t = 4.65 s. From the results of the free-surface elevations and the velocity fields, the velocity in the numerical simulation can be clearly differentiated into two portions, which is similar to the effect caused by the boundary layer in the numerical simulation of a bore uprush the smooth slope. This shows that the flow patterns of the simulated bore are qualitatively similar to those of the bore generated in the laboratory experiments, which suggests that

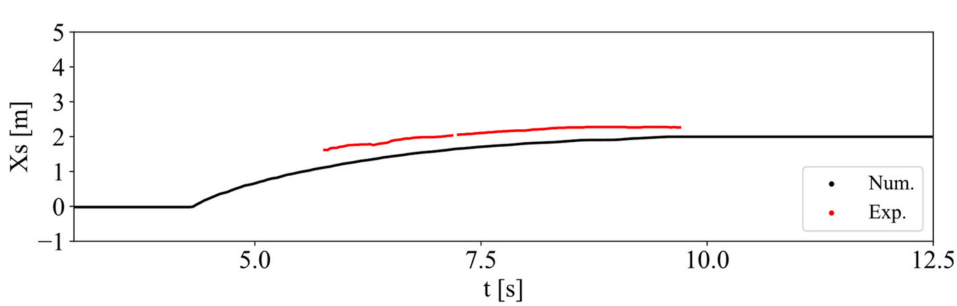

Fig. 9. Model–data comparison of inundation distance in time series for the Type A configuration of macro-roughness slope, where $h_1/h_0 = 30/10$ and $h_0 = 10$ cm.

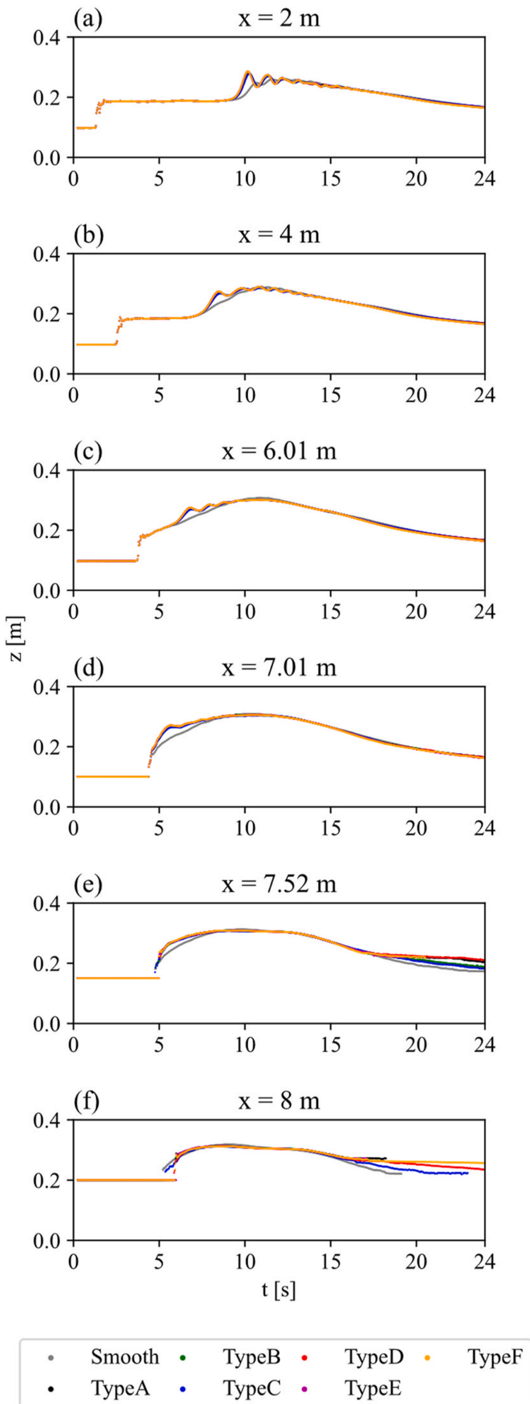

Fig. 10. Comparison of simulated free-surface elevation in time series for different macro-roughness slope configurations, where $h_1/h_0 = 30/10$ and $h_0 =$ 10 cm.

the propagation of the bore proceeds in a similar fashion in both the numerical and experimental simulations. However, owing to the limitations inherent in the experimental setup, the velocity distribution of the bore can only be determined using numerical simulations.

4.2.3. Inundation distance

A model–data comparison of the inundation distance in time histories is shown in Fig. 9 for the Type A configuration of the macro-roughness slope. However, similar to the smooth case, the numerically simulated results are consistently lower than those observed in the experimental data. More specifically, the measured and modeled maximum inundation distances are 2.27 m and 2.00 m, respectively, resulting in a relative error of 12%. Such underestimations of the simulated runup heights are found for both the smooth case (see Fig. 6) and the macro-roughness case (see Fig. 9). The reason for this error seems to be identical to that in the smooth slope case. The boundary condition is probably one of the main factors affecting the simulation results.

Although the simulated runup heights are lower than those of the measured results, the estimated errors are most likely similar. Thus, the numerically simulated results using DualSPHysics can still be used and exercised cautiously while keeping the anticipated errors in mind. Apart from underestimation of runup heights, the overall inundation in the time series was properly simulated.

4.3. Additional numerical simulations

The numerical model was validated for the macro-roughness slope of one configuration. Then, it was employed to clarify the effects of different arrangements of elements on the uprush processes and resulting runup heights. Using the same particle size and boundary conditions, five additional configurations of macro-roughness slope were simulated for $h_1/h_0 = 30/10$ and $h_0 = 10$ cm. As mentioned in Section 3.2, the projected areas occupied by the elements of the six macro-roughness slopes are identical. As such, the changes in the arrangements of the allocated elements in practical applications can be regarded as different planning schemes for buildings and streets in waterfront areas.

Fig. 10 shows a comparison of the free-surface elevation time series for the six macro-roughness slopes and the smooth slope case. In this plot, the free-surface elevations of the six macro-roughness slopes are nearly the same for the first three wave gauges located in the constant depth region, i.e., x < 6.01 m [Fig. 10 (a)–(b)], and the toe of the slope, i.e., x = 6.01 m [Fig. 10 (c)], which means that the incoming bore was not affected by macro-roughness elements. The reflected waves were influenced by the elements based on the recordings of the wave gauges. Noticeable variations were observed in the swash zone, i.e., x = 7.01 m [Fig. 10 (d)], x = 7.52 m [Fig. 10 (e)], and x = 8 m [Fig. 10 (f)]. Such variations in free-surface fluctuations caused by the presence of different macro-roughness configurations are the main factors affecting the inundation distance. Clearly, the incoming bore reaching x = 8 m was delayed for Types D, E and F [Fig. 10 (f)].

Fig. 11 shows the time history of the inundation distance, in which the smooth case is regarded as the reference case to calculate the runup reduction rate. In Fig. 11, for the six macro-roughness slopes, the overall trends of the inundation time series are mostly the same, in which the maximum runup heights occur almost simultaneously; however, the levels of inundation distance are case-dependent. More specifically, the inundation process and maximum inundation distance (i.e., corresponding to the maximum runup heights) for the Type B and Type C configurations are mostly the same, in which the former is slightly higher than the latter at t < 10 s whereas the inundation characteristics for the Type E and Type F configurations are similar. Also, the inundation curves in the time series for the Type A and Type D cases are similar when the maximum runup heights are reached.

In terms of the maximum runup height, we present a quantitative comparison using the runup reduction rate. This reduction rate is defined as $\gamma = 1 - R_{rough}/R_{smooth}$, where R_{rough} and R_{smooth} are the maximum runup heights of the rough and smooth slopes, respectively. The corresponding maximum inundation distances for all the simulated cases are listed in Table 1, and their values are rounded off to the 2nd decimal place for brevity. The reduction rates for the six macro-roughness slopes ranged from 12% to 25%. Specifically, the Type A and Type D cases can reduce by 17% to 18% when compared to that achieved by the smooth case, whereas the Type B and Type C cases can reduce by approximately 12% with respect to the smooth slope situation. Furthermore, the rotated arrangements (in relation to the flow

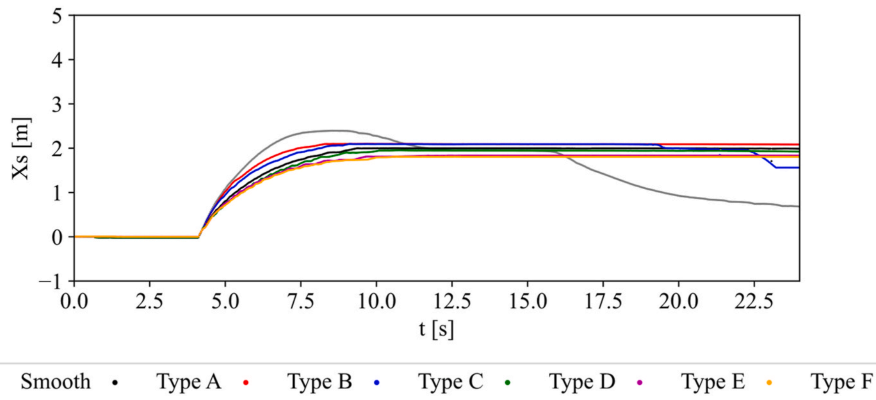

Fig. 11. Comparison of numerically simulated inundation distance in time series for different macro-roughness slope configurations, where $h_1/h_0 = 30/10$ and $h_0 =$ 10 cm.

Table 1
Details of the maximum inundation distance and the corresponding reduction rates for all macro-roughness slope configurations, where $h_1/h_0 = 30/10$ and h_0 = 10 cm.

Type	Maximum inundation distance (m)	Reduction rate with respect to the smooth case (γ)
Smooth	2.39	–
A	2.00	16.5%
B	2.10	12.3%
C	2.10	12.4%
D	1.95	18.4%
E	1.84	23.2%
F	1.80	24.6%

direction), Types E and Type F, can reduce by approximately 25% as compared to the smooth case, which shows their advantage in mitigating runup heights when attacked by a tsunami. The reduction rates were estimated based on the conditions considered in this study.

To further quantify the hydrodynamic variations for different cases, the maximum depth-averaged velocities in the x-direction were extracted from three selected points for each configuration (see Fig. 12). A general rule was held for selecting these points: the first point was selected at the gap of the first row and column of elements, the second was the point right behind the first selected point which was free of cube in the lateral direction, and the third point was selected next to the second one and shielded by the front macro-roughness element. As shown in Fig. 13, the larger the spaces between the elements, i.e., the street between the buildings in the waterfront area, the higher the flow velocity, which allows the flow to inundate further inland. However, noticeable increments of velocities could be found at the third points for Types E and F whose gaps between the elements were relatively narrower than the other types. The behaviors between different configuration types were varied owing to the change of the flow path.

The impact of the arrangement of the macro-roughness elements on the path along which the water uprushes the slope can be seen in Fig. 14. The gaps between the structures in the Type B and Type C configurations are larger than those in Types A, D, E and F, thus allowing more water to flow through the first few arrays of elements. Owing to the effects of the free-surface, the velocity of the flow passing through the larger gaps in Types B and C is higher than that in Types A and D. The uprush flows are largely affected by Types E and F because of the relatively small gaps between neighboring elements, which corresponds to the analysis in Fig. 13.

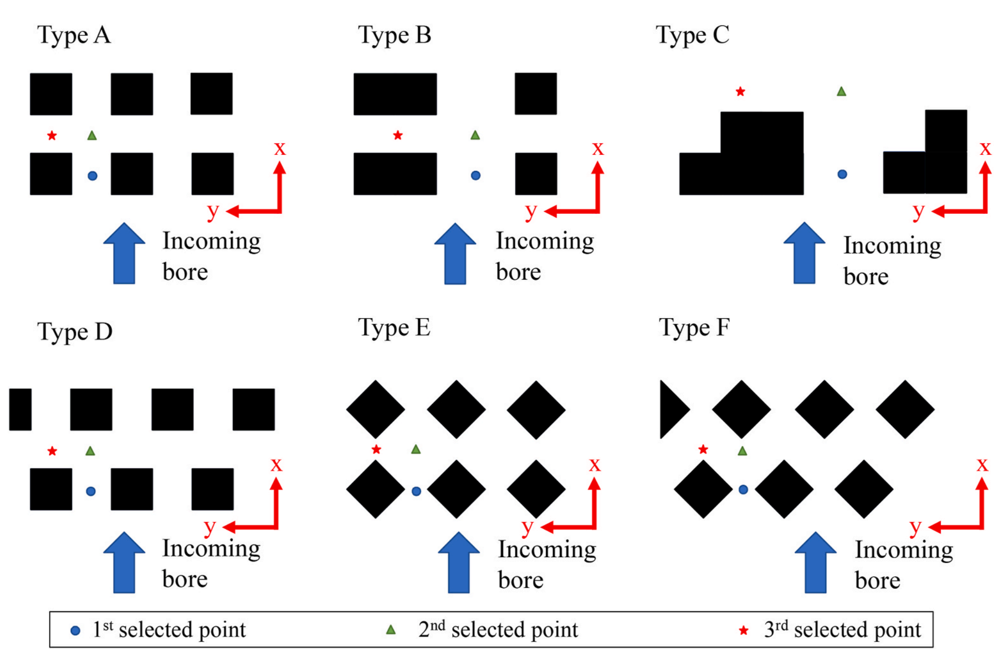

Fig. 12. Diagram of the points selected to analyze the velocity variations owing to the presence of the macro-roughness elements.

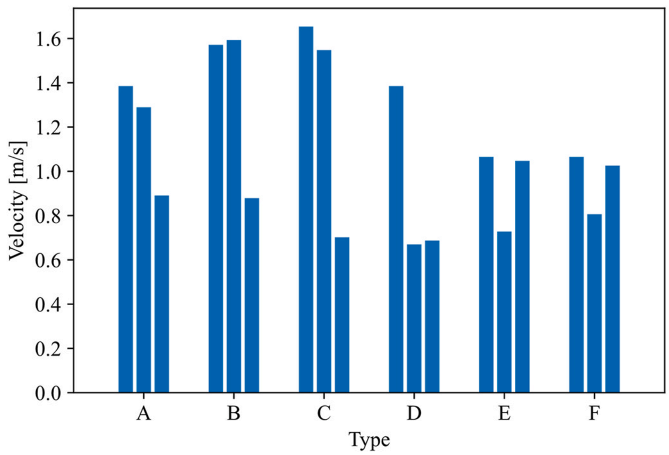

Fig. 13. The maximum depth-averaged velocities in the x-direction at the selected points for all the cases. In this histogram, the bar graph from the left to the right for each macro-roughness type represents the first, second and third selected points, respectively.

Moreover, Fig. 11 shows that the time when the flow starts to retreat for the smooth slope case, i.e., t > 10 s, is earlier than that the macro-roughness slope cases, indicating that the period of inland inundation for a macro-roughness slope remains longer than that for a smooth slope. Fig. 14 shows the simulated flow patterns at a specific runup stage at t = 7 s for the six macro-roughness configurations and Fig. 15 presents the simulated flow patterns at the rundown stage at t = 18 s for the six cases. The maximum depth-averaged velocities during rundown processes were shown in Fig. 16, which presents the retreating velocities at the same selected points depicted in Fig. 12. The rundown flow velocities tend to be larger at the gaps in Types A, B and C, whose paths created by the gaps surrounded by elements are straight. On the other hand, the backwash velocities maintain approximately similar order of magnitude for Types D, E and F, whose paths are relatively meander and narrow. One of the anticipated consequences is that the inundation caused by a tsunami-like bore may be prolonged due to the presence of structures in waterfront areas. This phenomenon may be somewhat different from that in reality since the actual building may not be impermeable, and indeed features the effects of the porosity, and thereby the permeability. Further investigation should be conducted to explore these effects.

Bore-induced swash hydrodynamics are characterized by the bore length and bore strength. Barranco and Liu (2021) demonstrated that runup heights do not depend on bore length as long as the incoming bore features a non-decaying bore. The bore strength is the Froude number, $F = U_b/(gh_0)^{1/2}$, for a bore moving at a constant velocity U_b, in a constant depth region with an undisturbed depth of h_0. Therefore, the relationship between realistic tsunamis and small-scale experiments can be properly scaled using the bore length, i.e., the Froude number. In addition, the Reynolds similarity should be considered, where the Reynolds number can be defined as $Re = U_b h_0/\nu$. Barranco and Liu (2021) reported that, based on observations of the 2011 Japan tsunami in Kuji Bay (Nakagi et al., 2016), the bore strength is estimated to be $1.36 < F < 2$ at a 10 m water depth and the Reynolds numbers are in the range of $10^8 < Re < 2 \times 10^8$, revealing that the flows are in the fully developed turbulent region, i.e., $Re > 10^4$ (Hughes, 1993). For the selected experimental conditions (Huang and Wu, 2021) used in this study, the Reynolds number and the Froude number of non-decaying dambreak-generated bores are within the range of $1.48 \times 10^5 < Re < 1.67 \times 10^5$ and $1.50 < F < 1.69$, respectively. Consequently, the bore-induced flow remains turbulent, and the bore strength is similar to that of realistic tsunamis. Furthermore, Wu et al. (2018) showed that the runup height data obtained from large-scale and small-scale experiments for both solitary and periodic waves collapsed on the same dimensionless runup height trend, indicating a weak dependency on the Reynolds number when turbulent flow conditions were studied. Considering a water depth of 10 m (e.g., Nakagi et al., 2016), the experiments with a water depth of 0.1 m can be regarded as an idealized 1/100 length scale model to prototype, for which the Froude similitude is followed. The abovementioned evidence suggests that the experimental and simulated bore characteristics considered herein can be

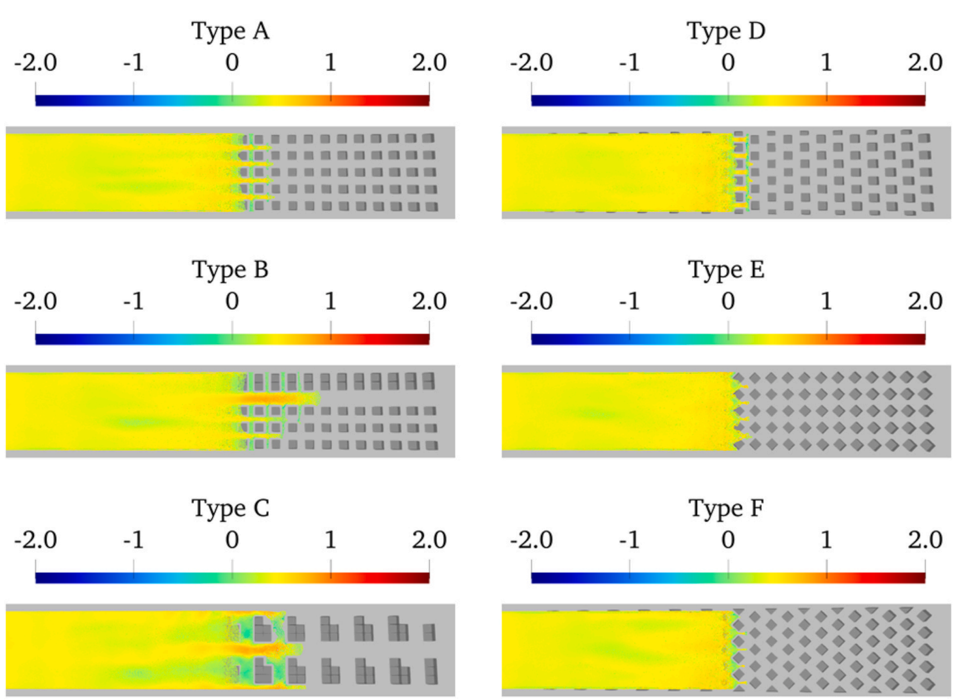

Fig. 14. Comparison of numerically simulated flow patterns in the x-y plane for different macro-roughness slope configurations, where $h_1/h_0 = 30/10$ and $h_0 = 10$ cm. All snapshots are consistently extracted at t = 7 s for different configurations during the stage of bore uprush. The colorbar indicates the simulated velocities (m/s) of particles in the x-direction.

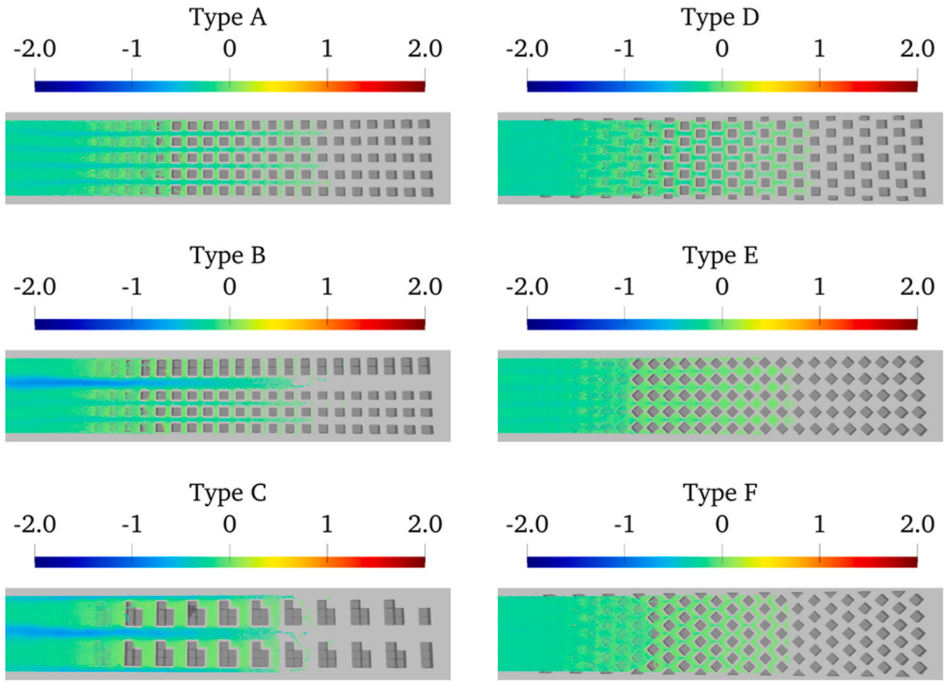

Fig. 15. Comparison of numerically simulated flow patterns in the x-y plane for different macro-roughness slope configurations, where $h_1/h_0 = 30/10$ and $h_0 = 10$ cm. All snapshots are consistently extracted at t = 18 s for different configurations during the stage of bore downrush. The colorbar indicates the simulated velocities (m/s) of particles in the x-direction.

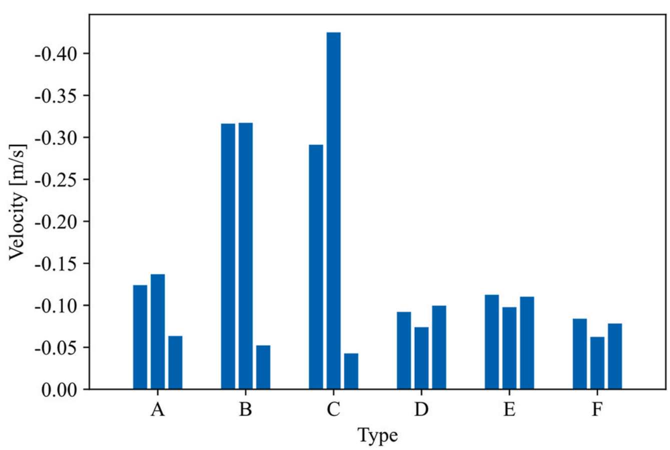

Fig. 16. The maximum depth-averaged velocities in the x-direction at the selected points for all the cases at t = 18 s. In this histogram, the bar graph from the left to the right for each macro-roughness type represents the first, second and third selected points, respectively.

related to field conditions. However, the application of the results in real-world scenarios should be exercised cautiously because using fixed cubes to model realistic buildings is an excessive simplification; thus, further investigation to model the movement and damage of structures triggered by long waves is desired.

5. Conclusions

In this study, dam-break driven swash flows on smooth and macro-roughness slopes were numerically studied using the open-source SPH program, DualSPHysics (Domínguez et al., 2022). The numerically simulated results were compared with available experiments for free-surface elevations, flow fields, inundation distances, and maximum runup heights.

For dam-break driven swash on a smooth slope, model–data comparison revealed that the numerical model can accurately predict the free-surface elevation in the constant depth region and in the surf zone, as well as in the swash zone. The free-stream flow velocities at the still-water shoreline were correctly captured by the numerical model, but the model failed to predict the flow velocities near the bottom boundary. This limitation further influenced the performance of numerical results in modeling the inundation as well as the runup processes. The overall trend of the inundation distance time series was similar between the measured and modeled results; however, the simulated results were consistently lower than that of the experiments. A 19% relative error of the modeled maximum runup height was obtained when compared with the experiment.

The effect of slope roughness was studied using macro-roughness features, which consisted of a smooth slope covered by a layer of cubes of the same size. This setup has implications for modeling flows passing through complicated geometries, such as buildings and streets in waterfront areas. For the bore-driven swash on the macro-roughness slope, model–data comparisons showed satisfactory agreement on the free-surface elevations and flow patterns. Again, the overall inundation distance in the time series was similar between the two results, but a consistent underestimation was observed in the modeled results, which led to a 12% relative error in the numerically simulated maximum runup height. Consequently, it is worthwhile to compare the results using different boundary conditions and turbulence models to improve the accuracy of the simulated results.

Additional numerical simulations with different arrangements of macro-roughness elements, whose projected areas on the slope were identical, were conducted to investigate their effects on runup heights. The numerical results revealed that the reduction rate of the maximum runup height varied for the six configurations considered in this study. The maximum runup height reduction was approximately 25% compared to the smooth slope case. Although the macro-roughness slope was able to reduce the level of inundation because the structures on the slope partially blocked the bore uprush, the inundation time for the macro-roughness slope cases was longer than that for the smooth slope case because the macro-roughness elements also influenced the bore downrush. This further confirms that the space between the elements is one of the main factors determining the extent of inundation.

Simulating a real-world scenario using numerical models is straightforward, but fully resolving the physics involved is complicated and requires rigorous model validation. Buildings and structures in waterfront areas may move and/or be damaged by long waves. The selection of different types of numerical models is a matter of choice when replicating complicated situations. Because the particle-based model has an advantage in modeling multi-phase flows dominated by complex boundary dynamics without mesh tangling issues, such as debris movement caused by flows or waves (e.g., Majtan et al., 2021), SPH may be an ideal tool to achieve the research topic mentioned above. This study can be further extended by considering the effects on element movements and even structure damages triggered by dam-break driven swash flows, with the aim of providing more insights into the hydrodynamic behavior of tsunami-like long waves in waterfront areas.

CRediT authorship contribution statement

Chun-Cheng Chang: Conceptualization, Methodology, Investigation, Writing – original draft, Writing – review & editing. **Yun-Ta Wu:** Conceptualization, Investigation, Funding acquisition, Writing – original draft, Writing – review & editing.

Declaration of competing interest

The authors declare that they have no known competing financial interests or personal relationships that could have appeared to influence the work reported in this paper.

Data availability

Data will be made available on request.

Acknowledgments

This study was financially supported by the National Science and Technology Council, Taiwan (108-2218-E-006-053-MY3 and 111-2221-E-006-091-MY2) and, in part, by the Higher Education Sprout Project, Ministry of Education to the Headquarters of University Advancement at the National Cheng Kung University. The authors are grateful to the anonymous reviewers, whose valuable comments and suggestions have improved the quality of this paper.

Appendix A. Effects on numerical simulations

A.1 Effect of particle sizes in simulations

The numerical results obtained using three different particle sizes $dp = 0.001$, 0.005, and 0.01 m were compared with the measured data. Figure A1 shows a comparison between the SPH simulated results using these different particle resolutions and experimental results. The comparison shows that the use of $dp = 0.001$ and 0.005 m produces similar results while the use of $dp = 0.01$ m shows a delay of the incoming bore. Therefore, for the dam-break conditions simulated herein, a particle resolution of $dp = 0.005$ m was satisfactory. However, $dp = 0.001$ m was employed in 2D to provide better resolution in space compared with the measured velocity fields.

A.2 Effect of 2D and 3D simulations

Figure A2 compares the time histories of the free-surface elevations between the 2D and 3D simulations for the smooth-slope case. In these two cases, the particle size of $dp = 0.005$ m is used. The results show that noticeable variations can be found near the bore front at the initial stage of the bore development, i.e., $x = 2$ and 4 m at $t < 4$ s. At the toe of the slope ($x = 6.01$ m) and in the swash zone ($x = 7.01$ and 7.52 m), the 2D and 3D simulated results were mostly identical. Figure A3 shows the inundation distance in time series, where the maximum inundation is $X_s = 2.30$ and 2.39 m for the 2D and 3D cases, respectively. Because the 3D simulation involves the interactions of fluid particles in the lateral direction, their hydrodynamic characteristics are not entirely the same (e.g., Wu et al., 2021) and therefore a variation of approximately 4% in the inundation distance between the 2D and 3D results should be acceptable.

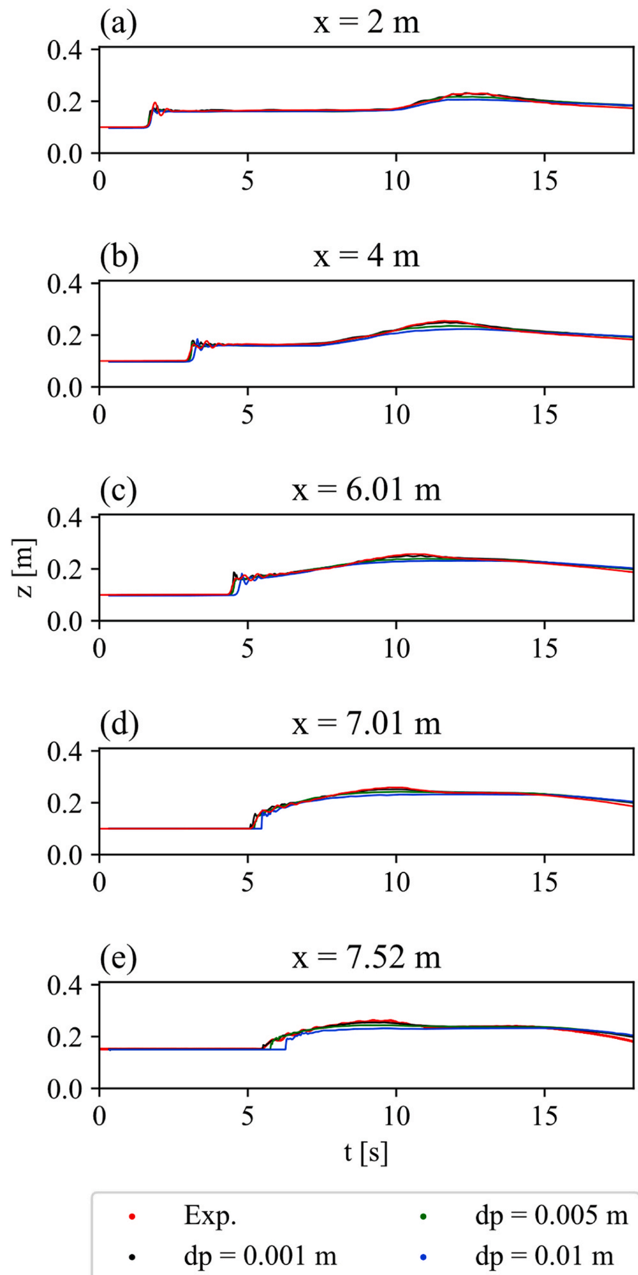

Figure A1. Model–data comparison of free-surface elevation in time series at different locations for dam-break driven swash on the smooth slope, where $h_1/h_0 = 24/10$ and $h_0 = 10$ cm. In this plot, experimental data are compared with numerical results using three different particle sizes.

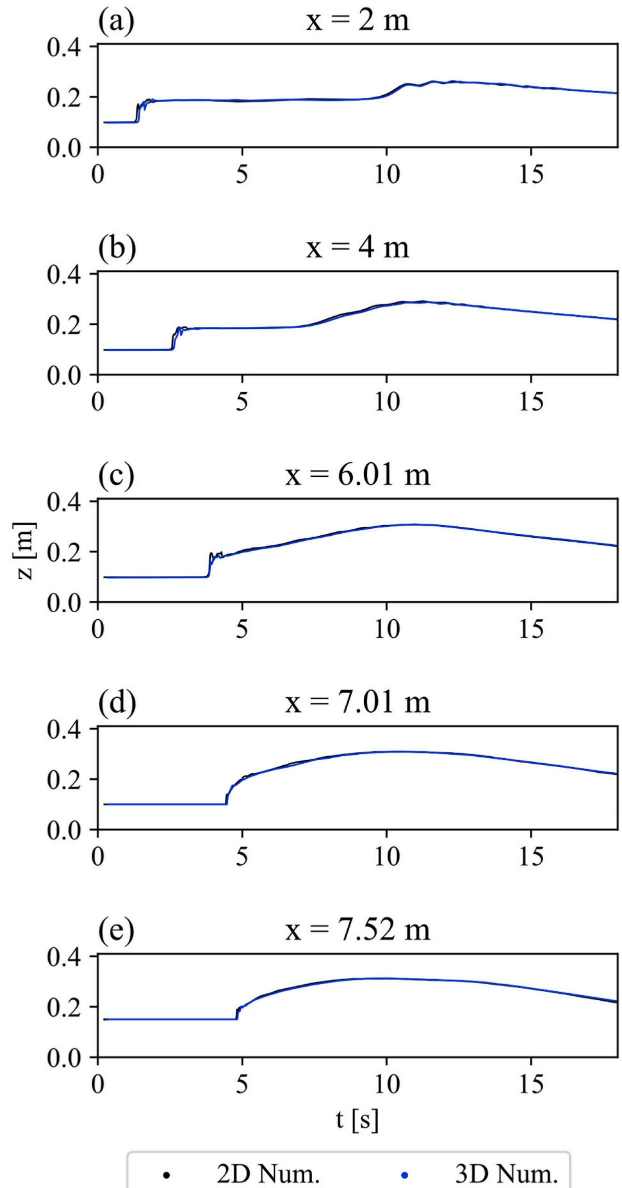

Figure A2. Comparison of free-surface elevation in time series between 2D and 3D simulations for dam-break driven swash on the smooth slope, where $h_1/h_0 = 30/10$ and $h_0 = 10$ cm.

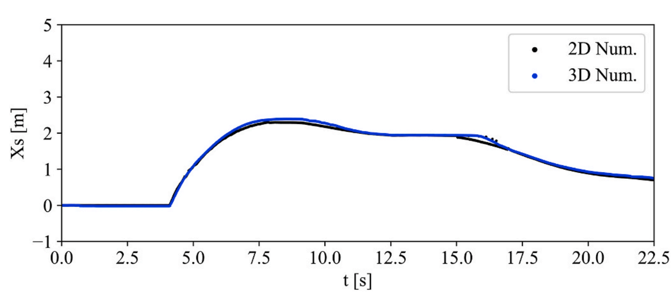

Figure A3. Comparison of inundation distance in time series between 2D and 3D simulations for dam-break driven swash on the smooth slope, where $h_1/h_0 = 30/10$ and $h_0 = 10$ cm.

References

Altomare, C., Crespo, A.J.C., Domínguez, J.M., Gómez-Gesteira, M., Suzuki, T., Verwaest, T., 2015. Applicability of smoothed particle hydrodynamics for estimation of sea wave impact on coastal structures. Coast. Eng. 96, 1–12.

Antuono, M., Colagrossi, A., Marrone, S., 2012. Numerical diffusive terms in weakly-compressible SPH schemes. Comput. Phys. Commun. 183 (12), 2570–2580.

Asai, M., Miyagawa, Y., Idris, N., Muhari, A., Imamura, F., 2016. Coupled tsunami simulations based on a 2D shallow-water equation-based finite difference method and 3D incompressible smoothed particle hydrodynamics. Journal of Earthquake and Tsunami 10 (5), 1640019.

Barranco, I., Liu, P.L.-F., 2021. Runup and inundation generated by non-decaying dam-break bores on a planar beach. J. Fluid Mech. 915, A81.
Briggs, M.J., Synolakis, C.E., Harkins, G.S., Green, D.R., 1995. Laboratory experiments of tsunami runup on a circular island. Pure Appl. Geophys. 144 (3), 569–593.
Chan, I.-C., Liu, P.L.-F., 2012. On the runup of long waves on a plane beach. J. Geophys. Res. 117, C08006.
Chang, K.-A., Hsu, T.-J., Liu, P.L.-F., 2005. Vortex generation and evolution in water waves propagating over a submerged rectangular obstacle: Part II. Cnoidal waves. Coast. Eng. 52 (3), 257–283.
Chen, Y.-K., Liu, Y., Meringolo, D.D., Hu, J.-M., 2023. Study on the hydrodynamics of a twin floating breakwater by using SPH method. Coast. Eng. 179, 104230.
Chorin, A.J., 1968. Numerical solution of the Navier–Stokes equations. Math. Comput. 22 (104), 745–762.
Chuang, W.-L., Chang, K.-A., Kaihatu, J., Cienfuegos, R., Mokrani, C., 2020. Experimental study of force, pressure, and fluid velocity on a simplified coastal building under tsunami bore impact. Nat. Hazards 103 (1), 1093–1120.
Crespo, A.J.C., Domínguez, J.M., Rogers, B.D., Gómez-Gesteira, M., Longshaw, S., Canelas, R., Vacondio, R., Barreiro, A., García-Feal, O., 2015. DualSPHysics: open-source parallel CFD solver based on smoothed particle hydrodynamics (SPH). Comput. Phys. Commun. 187, 204–216.
Crespo, A.J.C., Gomez-Gesteira, M., Dalrymple, R.A., 2007. Boundary conditions generated by dynamic particles in SPH methods. Cmc-Computers Materials & Continua 5 (3), 173–184.
Domínguez, J.M., Fourtakas, G., Altomare, C., Canelas, R.B., Tafuni, A., García-Feal, O., Martínez-Estévez, I., Mokos, A., Vacondio, R., Crespo, A.J.C., Rogers, B.D., Stansby, P.K., Gómez-Gesteira, M., 2022. DualSPHysics: from fluid dynamics to multiphysics problems. Comput. Particle Mech. 9 (5), 867–895.
English, A., Domínguez, J.M., Vacondio, R., Crespo, A.J.C., Stansby, P.K., Lind, S.J., Chiapponi, L., Gómez-Gesteira, M., 2022. Modified dynamic boundary conditions (mDBC) for general-purpose smoothed particle hydrodynamics (SPH): application to tank sloshing, dam break and fish pass problems. Comput. Particle Mech. 9 (5), 1–15.
Fourtakas, G., Vacondio, R., Alonso, J.D., Rogers, B.D., 2020. Improved density diffusion term for long duration wave propagation. In: 2020 SPHERIC Harbin International Workshop, pp. 351–357. China.
Gingold, R.A., Monaghan, J.J., 1977. Smoothed particle hydrodynamics: theory and application to non-spherical stars. Mon. Not. Roy. Astron. Soc. 181 (3), 375–389.
Gomez-Gesteira, M., Rogers, B.D., Dalrymple, R.A., Crespo, A.J., 2010. State-of-the-art of classical SPH for free-surface flows. J. Hydraul. Res. 48 (Suppl. 1), 6–27.
Goseberg, N., 2013. Reduction of maximum tsunami run-up due to the interaction with beachfront development – application of single sinusoidal waves. Nat. Hazards Earth Syst. Sci. 13 (11), 2991–3010.
Gu, S., Zheng, W., Wu, H., Chen, C., Shao, S., 2022. DualSPHysics simulations of spillway hydraulics: a comparison between single- and two-phase modelling approaches. J. Hydraul. Res. 60 (5), 835–852.
Higuera, P., Liu, P.L.-F., Lin, C., Wong, W.-Y., Kao, M.-J., 2018. Laboratory-scale swash flows generated by a non-breaking solitary wave on a steep slope. J. Fluid Mech. 847, 186–227.
Hsiao, Y., Wu, Y.-T., 2022. Experiments on dambreak-generated bore over mobile slopes. In: Proceedings of the 23rd Ocean and Underwater Technology Conference in Taiwan, pp. 281–285 (in Chinese).
Huang, Y.-C., Wu, Y.-T., 2021. Runup of dambreak-generated bore on a rough slope. In: Proceedings of the 43rd Ocean Engineering Conference in Taiwan, pp. 38–43 (in Chinese).
Hughes, S.A., 1993. Physical Models and Laboratory Techniques in Coastal Engineering. World Scientific.
Khayyer, A., Shimizu, Y., Gotoh, H., Hattori, S., 2021. Multi-resolution ISPH-SPH for accurate and efficient simulation of hydroelastic fluid-structure interactions in ocean engineering. Ocean Eng. 226, 108652.
Kikkert, G.A., O'Donoghue, T., Pokrajac, D., Dodd, N., 2012. Experimental study of bore-driven swash hydrodynamics on impermeable rough slopes. Coast. Eng. 60, 149–166.
Kikkert, G.A., Pokrajac, D., O'Donoghue, T., Steenhauer, K., 2013. Experimental study of bore-driven swash hydrodynamics on permeable rough slopes. Coast. Eng. 79, 42–56.
Kim, Y., Zhou, Z., Hsu, T.-J., Puleo, J.A., 2017. Large eddy simulation of dam-break-driven swash on a rough-planar beach. J. Geophys. Res.: Oceans 122 (2), 1274–1296.
Li, Y., Raichlen, F., 2003. Energy balance model for breaking solitary wave runup. J. Waterw. Port, Coast. Ocean Eng. 129 (2), 47–59.
Lin, C., Kao, M.-J., Yuan, J.-M., Raikar, R.V., Hsieh, S.-C., Chuang, P.-Y., Syu, J.-M., Pan, W.-C., 2020. Similarities in the free-surface elevations and horizontal velocities of undular bores propagating over a horizontal bed. Phys. Fluids 32 (6), 063605.
Lin, P., Liu, P.L.-F., 1998. A numerical study of breaking waves in the surf zone. J. Fluid Mech. 359, 239–264.
Liu, P.L.-F., Cho, Y.-S., Briggs, M.J., Kanoglu, U., Synolakis, C.E., 1995. Runup of solitary waves on a circular Island. J. Fluid Mech. 302, 259–285.
Lo, E.Y.M., Shao, S., 2002. Simulation of near-shore solitary wave mechanics by an incompressible SPH method. Appl. Ocean Res. 24 (5), 275–286.
Lucy, L.B., 1977. A numerical approach to the testing of the fission hypothesis. Astron. J. 82, 1013–1024.
Luo, M., Khayyer, A., Lin, P., 2021. Particle methods in ocean and coastal engineering. Appl. Ocean Res. 114, 102734.
Madsen, P.A., Fuhrman, D.R., Schäffer, H.A., 2008. On the solitary wave paradigm for tsunamis. J. Geophys. Res. 113, C12012.
Majtan, E., Cunningham, L.S., Rogers, B.D., 2021. Flood-induced hydrodynamic and debris impact forces on single-span masonry arch bridge. J. Hydraul. Eng. 147 (11), 04021043.
Miller, R.L., 1968. Experimental determination of run-up of undular and fully developed bores. J. Geophys. Res. 73 (14), 4497–4510.
Monaghan, J.J., 1992. Smoothed particle hydrodynamics. Annu. Rev. Astron. Astrophys. 30 (1), 543–574.
Monaghan, J.J., 1994. Simulating free surface flows with SPH. J. Comput. Phys. 110 (2), 399–406.
Monaghan, J.J., 2005. Smoothed particle hydrodynamics. Rep. Prog. Phys. 68 (8), 1703.
Monaghan, J.J., Kos, A., Issa, N., 2003. Fluid motion generated by impact. J. Waterw. Port, Coast. Ocean Eng. 129 (6), 250–259.
Moris, J.P., Kennedy, A.B., Westerink, J.J., 2021. Tsunami wave run-up load reduction inside a building array. Coast. Eng. 169, 103910.
Nóbrega, J.D., Matos, J., Schulz, H.E., Canelas, R.B., 2020. Smooth and stepped spillway modeling using the SPH method. J. Hydraul. Eng. 146 (8), 04020054.
Nakagi, T., Kosa, K., Sato, T., 2016. Evaluation of properties of tsunami in the Kuji port. J. Japan Soc. Civil Eng., Ser. B2 (Coast. Eng.) 72, 1033–1038.
Ng, K.C., Alexiadis, A., Chen, H., Sheu, T.W.H., 2020. A coupled smoothed particle hydrodynamics-volume compensated particle method (SPH-VCPM) for fluid structure interaction (FSI) modelling. Ocean Eng. 218, 107923.
O'Donoghue, T., Kikkert, G.A., Pokrajac, D., Dodd, N., Briganti, R., 2016. Intra-swash hydrodynamics and sediment flux for dambreak swash on coarse-grained beaches. Coast. Eng. 112, 113–130.
O'Donoghue, T., Pokrajac, D., Hondebrink, L.J., 2010. Laboratory and numerical study of dambreak-generated swash on impermeable slopes. Coast. Eng. 57 (5), 513–530.
Pintado-Patiño, J.C., Puleo, J.A., Krafft, D., Torres-Freyermuth, A., 2021. Hydrodynamics and sediment transport under a dam-break-driven swash: an experimental study. Coast. Eng. 170, 103986.
Pintado-Patiño, J.C., Torres-Freyermuth, A., Puleo, J.A., Pokrajac, D., 2015. On the role of infiltration and exfiltration in swash zone boundary layer dynamics. J. Geophys. Res.: Oceans 120 (9), 6329–6350.
Prasetyo, A., Yasuda, T., Miyashita, T., Mori, N., 2019. Physical modeling and numerical analysis of tsunami inundation in a coastal city. Front. Built. Eviron. 5, 46.
Qin, X., Motley, M.R., Marafi, N.A., 2018. Three-dimensional modeling of tsunami forces on coastal communities. Coast. Eng. 140, 43–59.
Roselli, R.A.R., Vernengo, G., Brizzolara, S., Guercio, R., 2019. SPH simulation of periodic wave breaking in the surf zone - a detailed fluid dynamic validation. Ocean Eng. 176, 20–30.
Schimmels, S., Sriram, V., Didenkulova, I., 2016. Tsunami generation in a large scale experimental facility. Coast. Eng. 110, 32–41.
Shadloo, M.S., Weiss, R., Yildiz, M., Dalrymple, R.A., 2015. Numerical simulation of long wave runup for breaking and nonbreaking waves. Int. J. Offshore Polar Eng. 25 (1), 1–7.
Shao, S., Lo, E.Y.M., 2003. Incompressible SPH method for simulating Newtonian and non-Newtonian flows with a free surface. Adv. Water Resour. 26 (7), 787–800.
Simamora, C., Shigihara, Y., Fujima, K., 2007. Experimental study on tsunami forces acting on structures. In: Proceedings of Coastal Engineering, JSCE. Japan Society of Civil Engineers, pp. 831–835.
Takahashi, K., Tomita, T., 2013. Simulation of the 2011 Tohoku tsunami in Kuji bay using three-dimensional non-hydrostatic numerical model. J. Japan Soc. Civil Eng., Ser. B2 (Coast. Eng.) 69, 166–170.
Torres-Freyermuth, A., Puleo, J.A., Pokrajac, D., 2013. Modeling swash-zone hydrodynamics and shear stresses on planar slopes using Reynolds-Averaged Navier–Stokes equations. J. Geophys. Res.: Oceans 118 (2), 1019–1033.
Verlet, L., 1967. Computer "experiments" on classical fluids. I. Thermodynamical properties of Lennard-Jones molecules. Phys. Rev. 159 (1), 98–103.
Violeau, D., 2012. Fluid Mechanics and the SPH Method: Theory and Applications. Oxford University Press.
Violeau, D., Issa, R., 2007. Numerical modelling of complex turbulent free-surface flows with the SPH method: an overview. Int. J. Numer. Methods Fluid. 53 (2), 277–304.
Wang, D., Liu, P.L.F., 2022. An ISPH with modified k–ε closure for simulating breaking periodic waves. Coast. Eng. 178, 104191.
Wei, Z., Dalrymple, R.A., Hérault, A., Bilotta, G., Rustico, E., Yeh, H.H., 2015. SPH modeling of dynamic impact of tsunami bore on bridge piers. Coast. Eng. 104, 26–42.
Wendland, H., 1995. Piecewise polynomial, positive definite and compactly supported radial functions of minimal degree. Adv. Comput. Math. 4 (1), 389–396.
Wu, Y.-T., 2022. Modeling the evolution and runup of breaking solitary and solitary-like waves on straight and composite slopes. Journal of Earthquake and Tsunami 16 (6), 2241003.
Wu, Y.-T., Higuera, P., Liu, P.L.-F., 2021. On the evolution and runup of a train of solitary waves on a uniform beach. Coast. Eng. 170, 104015.
Wu, Y.-T., Huang, K.-W., Kobayashi, N., 2022. Runup of breaking solitary waves on rough uniform slopes. Ocean Eng. 245, 110551.
Wu, Y.-T., Huang, Y.-C., 2020. Runup of dambreak-generated bore on a smooth slope. In: Proceedings of the 42nd Ocean Engineering Conference in Taiwan, pp. 209–214 (in Chinese).
Wu, Y.-T., Liu, P.L.-F., Hwang, K.-S., Hwung, H.-H., 2018. Runup of laboratory-generated breaking solitary and periodic waves on a uniform slope. J. Waterw. Port, Coast. Ocean Eng. 144 (6), 04018023.
Wu, Y.-T., Yeh, C.-L., Hsiao, S.-C., 2014. Three-dimensional numerical simulation on the interaction of solitary waves and porous breakwaters. Coast. Eng. 85, 12–29.
Yeh, H.H., Liu, P., Briggs, M., Synolakis, C., 1994. Propagation and amplification of tsunamis at coastal boundaries. Nature 372 (6504), 353–355.

Yeh, H.H., Ghazali, A., Marton, I., 1989. Experimental study of bore run-up. J. Fluid Mech. 206, 563–578.
Zhang, Q., Liu, P.L.F., 2008. A numerical study of swash flows generated by bores. Coast. Eng. 55 (12), 1113–1134.
Zhang, Z., Kennedy, A.B., Moris, J.P., 2023. Tsunami wave loading on a structural array behind a partial wall. Coast. Eng. 179, 104244.